Springer

KSME

Journal of Mechanical Science and Technology 30 (8) (2016) 3441~3452
www.springerlink.com/content/1738-494x(Print)/1976-3824(Online)
DOI 10.1007/s12206-016-0702-8

The meshing angular velocity and tangential contact force simulation for logarithmic spiral bevel gear based on Hertz elastic contact theory†

Tieming Xiang[1,2], Lizhi Gu[1,*] and Jianmin Xu[1,2]

[1]*College of Mechanical Engineering and Automation, Huaqiao University, Xiamen, 361021, China*
[2]*School of Mechanical & Automotive Engineering, Xiamen University of Technology. Xiamen, 361024, China*

(Manuscript Received May 25, 2015; Revised April 10, 2016; Accepted April 19, 2016)

Abstract

To obtain the change tendency of output angular velocity and tangential contact force of a gear when the pinion under the step input during meshing of a new type of spiral bevel gear, which is a logarithmic spiral bevel gear, the tooth flank equation of logarithmic spiral bevel gear is deduced based on the formation mechanism of the tooth flank formation. A three-dimensional model of a pair of logarithmic spiral bevel gears whose number of teeth was 37:9, with modules being 4.5 mm, normal pressure angle being 20 degrees and spiral angle being 35 degrees were built and assembled. Based on Hertz elastic contact theory, the calculation formulas and parameters sets of contact force for conventional spiral bevel gear meshing simulation and logarithmic spiral bevel gear meshing simulation were done. Consider the dynamic simulation about meshing angular velocity and tangential contact force for conventional spiral bevel gear meshing and logarithmic spiral bevel gear meshing, respectively. Finally, by analyzing and comparing the simulation data, the results show that under the same input conditions, the fluctuation of the gear angular velocity and tangential contact force of logarithmic spiral bevel gear meshing are smaller than the conventional spiral bevel gear. That is, the transmission stationary of logarithmic spiral bevel gear meshing is superior to conventional spiral bevel gear.

Keywords: Logarithmic spiral bevel gear; Three-dimensional modeling; Meshing angular velocity; Tangential contact force; Hertz elastic contact theory

---

1. Introduction

1.1 Spiral bevel gear and logarithmic spiral bevel gear

Spiral bevel gear (SBG), also called Gleason spiral bevel gear or curved tooth bevel gear, is widely used in various transmission fields, such as aerospace, machine tool, ship and automobile industry due to its outstanding features on smooth transmission, such as low noise and high coincidence ratio [1]. However, the spiral angle of the conventional SBG at a point is not equal everywhere because the conventional SBG spiral angle is usually defined by the nominal spiral angle of the midpoint of tooth trace line [2]. It is required for the value of spiral angle of meshing contact point to be equal for the purpose of increasing transmission stability, improving the tooth face contact state and elongating the service life.

The Logarithmic spiral bevel gear (LSBG) proposed in the Refs. [2-4] has the characteristic that the tooth trace line is a conical logarithmic spiral line, which has equal spiral angles at a point. However, the actual dynamic behavior of LSBG still needs to be studied and verified.

*Corresponding author. Tel.: +86 13110705113, Fax.: +86 592 6291588
E-mail address: gulizhi8882@163.com
†Recommended by Editor Yeon June Kang

1.2 Modeling about SBG

Generally speaking, there are three kinds of methods for conventional SBG modeling [5]. The first kind is a surface fit modeling based on tooth flank equation derivation [6-8]. This method first creates a discrete points solutions array of SBG tooth flank by using mathematical software such as Matlab, then generates a surface model through mathematical fitting of the discrete points solutions array, and finally builds a model through a surface model [9-13]. The second kind is simulation process modeling through virtual processing. Based on meshing equations, it uses a virtual simulation machine tool for processing to obtain the SBG three-dimensional (3D) model [17-24]. The third is make the tooth profile sweep along the tooth trace line direction to form a single tooth, then arrays the single tooth to build up the whole model [2] with a commercial software package such as UG, or Pro-E, or Catia. In this paper, we use the first method to accurately model.

1.3 Meshing angular velocity and contact force simulation of SBG

Mechanical engineers and specialists in mechanical fields [25-29] have done many researches on SBG vibration, shock and noise, which may be caused by the changes of angular velocity and contact force during meshing [30-34]. Litvin studied the contact problem of SBG by means of numerical analysis method, and proposed tooth contact analysis method based on "local synthesis method" [35-36]. Fong proposed the method of fourth-order comprehensive curve of SBG tooth flank meshing movement for building the mathematical model [37]. Yao carried out the modeling and simulating with double circular-arc SBG [38]. Velex simulated the dynamic behavior of bias planetary gear mechanism [39]. Chen did dynamics simulation of planetary gear and spur gear [40-42]. Fang proposed a precise modeling method of arc tooth face-gear with transition curve and did the kinematic analysis [43]. He also processed a prototype by CNC machine tool. Benamar undertook the quasi-static motion simulation and slip prediction of articulated planetary rovers by using kinematic approach [44]. Simon optimized the process of face-hobbed SBG on CNC hypoid gear generator [45]. There are many other scholars and engineers researched on the kinematics analysis, dynamic analysis and meshing contact analysis of spur gear [46-48], helical gear [49, 50], planetary gear [51-53], SBG, hypoid gear and so on. But there are few reports about simulation of meshing angular velocity and contact force of LSBG.

2. 3D Modeling of LSBG

2.1 Conical logarithmic spiral line

LSBG is a special SBG which uses the conical logarithmic spiral line as the tooth trace, and uses the involutes as tooth profile line. As shown in Fig. 1 the parameter equation of conical logarithmic spiral line [2] in the Cartesian coordinates is

$$\begin{cases} x = OM_x = ae^{\phi\sin\alpha\cot\beta}\sin\alpha\cos\phi \\ y = OM_y = ae^{\phi\sin\alpha\cot\beta}\sin\alpha\sin\phi \\ z = OM_z = ae^{\phi\sin\alpha\cot\beta}\cos\alpha \end{cases} \tag{1}$$

where a is the distance between the start point of the logarithmic spiral line and the top of the cone; ϕ is the independent variable which reflects the projection angle on the bottom plane of the moving points turning angle; α is the half angle of the cone and β is the spiral angle.

The projection of the conical logarithmic spiral line on the bottom plane is the plane logarithmic spiral line. The value of spiral angle between the conical logarithm spiral tangent direction and the cone element direction is a constant.

2.2 The process of tooth flank formation for LSBG

The tooth flank forming process of helical cylindrical gear is shown in Fig. 2.

A generate plane is rolling purely around the base cylinder. The space tooth flank surface is swept by a bias straight line on the generate plane.

The formation of SBG tooth flank is similar to helical cylindrical gear, which is swept by a conventional spiral line on the plane while the plane is rolling purely around the base cone. Now, replace the conventional spiral line on the plane with a conical logarithmic spiral line, generating a surface that sweeps by the logarithmic spiral line on the plane while the plane is rolling purely around the base cone is the LSBG tooth flank as shown in Fig. 3.

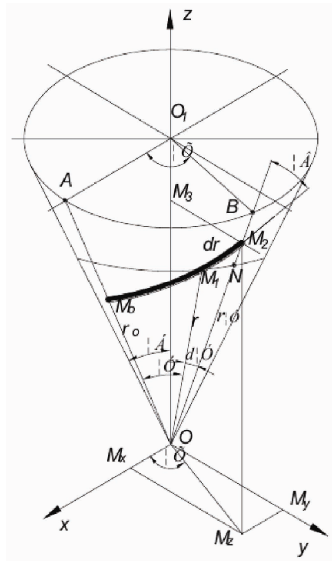

Fig. 1. Conical logarithmic spiral line.

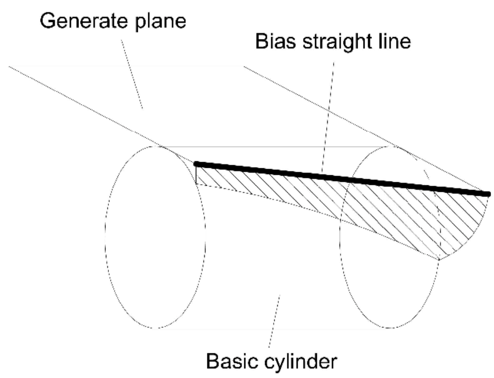

Fig. 2. The tooth flank formation mechanism of helical cylindrical gear.

2.3 The construction of tooth flank equations for LSBG

As shown in Fig. 4, the line OP is a tangent line between plane Q and base cone K with base cone angle θ, when the plane Q around base cone K does pure rolling expansion movement, a logarithmic spiral line MN on plane Q sweeps a surface in space which is the LSBG tooth flank. To get the tooth flank equation of LSBG, we establish two left-handed coordinates at the top point of O on base cone K for the circle center. One left-handed coordinates is O-xyz, which is fixedly connected with the base cone K. The other left-handed coordinate is $O-x'y'z'$ which is fixedly connected with the rota-

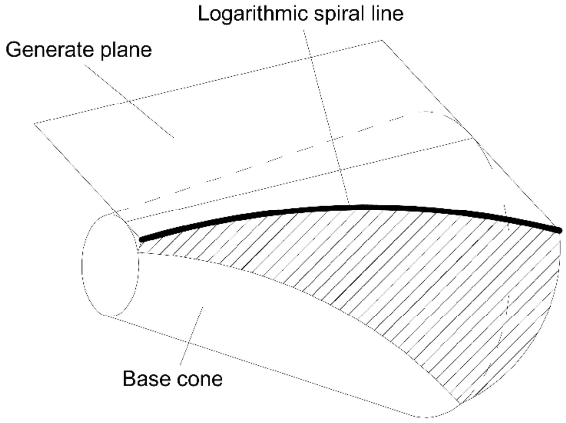

Fig. 3. The tooth flank formation mechanism of LSBG.

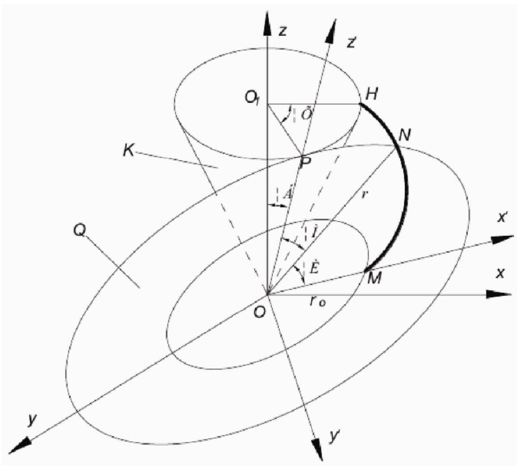

Fig. 4. The coordinates for tooth flank equation.

tion plane Q. The x' axis on the plane Q and z' axis with the OP direction is the instantaneous axis which plane Q is rolling purely along with the base cone K. The coordinate transformation formula from the coordinates $O-x'y'z'$ to the coordinates O-xyz can be expressed as follows:

$$\begin{cases} x' = x\sin\phi - y\cos\phi \\ y' = x\cos\alpha\cos\phi + y\cos\alpha\sin\phi - z\sin\alpha \\ z' = x\sin\alpha\cos\phi + y\sin\alpha\sin\phi + z\cos\alpha \text{ .} \end{cases} \tag{2}$$

The equations of logarithmic spiral line MN on the plane $x'Oz'$ can be written as follows:

$$\begin{cases} x' = r_0 e^{k\theta}\cos\theta \\ y' = 0 \\ z' = r_0 e^{k\theta}\sin\theta \end{cases} . \tag{3}$$

So, the incomplete parameter tooth flank equation of LSBG which contains the unknown parameter α can be expressed as follows:

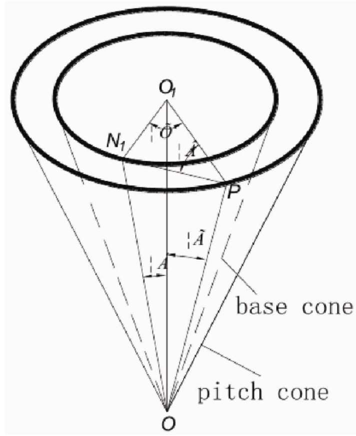

Fig. 5. The relationship between base cone angle and pitch cone angle.

$$\begin{cases} r_0 e^{k\theta}\cos\theta = x\sin\phi - y\cos\phi \\ 0 = x\cos\alpha\cos\phi + y\cos\alpha\sin\phi - z\sin\alpha \\ r_0 e^{k\theta}\sin\theta = x\sin\alpha\cos\phi + y\sin\alpha\sin\phi + z\cos\alpha \end{cases} . \tag{4}$$

The above LSBG tooth flank equation is an incomplete parameter equation because the base cone angle α is unknown. The base cone angle α must be calculated to determine LSBG complete tooth flank equation.

The base cone is smaller than the pitch cone because base cone angle α is smaller than pitch cone angle γ according to the mechanism of the LSBG tooth flank formation; that is, the base cone locates within the pitch cone. So, there must be an intersection line between the tooth flank which is formed by spreading the logarithmic spiral line on the base cone exterior transverse and pitch cone surface.

The angle between the two intersecting surface tangent planes which is the spiral angle of the meshing point according to the definition of SBG spiral angle as shown in Fig. 5. From the formation mechanism of spherical involutes tooth profile, O_1, N_1, P on the same spherical surface and forms the spherical triangle $\Delta O_1 N_1 P$, the sine formula of spherical geometry can be written as follows:

$$\sin\theta = \sin\beta\sin\gamma \text{ .} \tag{5}$$

The base cone angle α can be written as follows by derivation from Eq. (5).

$$\alpha = \arcsin(\sin\beta\sin\gamma) \text{ .} \tag{6}$$

In Eq. (6), β and γ are decided by the designer. The complete tooth flank equation of LSBG can be expressed as follows:

$$\begin{cases} r_0 e^{k\theta}\cos\theta = x\sin\phi - y\cos\phi \\ 0 = x\cos\alpha\cos\phi + y\cos\alpha\sin\phi - z\sin\alpha \\ r_0 e^{k\theta}\sin\theta = x\sin\alpha\cos\phi + y\sin\alpha\sin\phi + z\cos\alpha \\ \alpha = \arcsin(\sin\beta\sin\gamma) \text{ .} \end{cases} \tag{7}$$

Table 1. Some parameters for a pair of LSBGs.

Parameter	Symbol / Unit	Pinion	Gear
Number of teeth	z	9	37
Exterior transverse modulus	m/mm	4.5	4.5
Shaft angle	$\sum$/(°)	90	90
Rotation direction		Left	Right
Pitch circle diameter	d/mm	40.5	166.5
Pressure angle	α_n/(°)	20	20
Spiral angle	β_m/(°)	35	35
Addendum	h_a/mm	3.825	3.825
Dedendum	h_f/mm	4.671	4.671

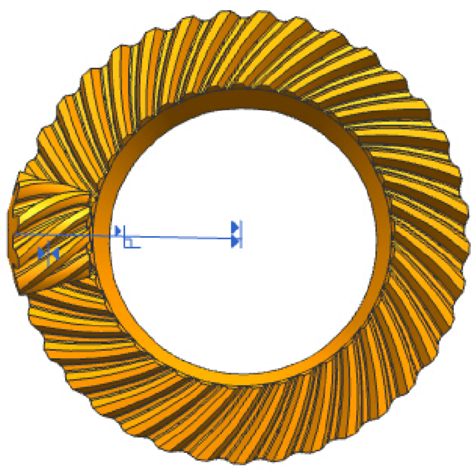

Fig. 6. The 3D model of LSBG.

2.4 The 3D model of a pair of LSBGs

Use LSBG pairs to replace SBG pairs on the main reduce transmission of a minibus main reducer. Some parameters of LSBG are shown in Table 1.

According to the related parameters in Table 1, the Matlab software package is employed to solve the discrete points on the LSBG tooth flank, fit the discrete points to generate tooth flank surface, and then create a tooth profile model. The LSBG 3D models of the pinion and gear were built by UG software package. The 3D assembly model of LSBG was built by three constraint conditions: the shaft angle $\sum = 90°$, the top point coincidence of the pinion and the gear, and the reference circle contact alignment of exterior transverse surface on the pinion and gear tooth flank. The 3D assembly model is shown in Fig. 6.

3. The meshing angular velocity and contact force simulation of LSBG

3.1 Basic formulas based on the Hertz elastic contact theory

Based on the Hertz elastic contact theory [54], the calculation formula of the contact force can be written in the form of

$$F = \begin{cases} kx^e + Step(x,0,0,d,C)\dot{x} & x < 0 \\ 0 & x \geq 0 \end{cases} \tag{8}$$

where F is the contact force, N; k is the coefficient of the contact stiffness, N/mm; x is a variable for the distance of two contact bodies, mm, x < 0 mean contact, x = 0 or x > 0 meaning not contact; e is the contact force index; function Step(x, 0, 0, d, C) is a piecewise function; C is damping coefficient, Ns/m and d is the contact maximum penetration depth, mm.

The calculation formula of stiffness k can be written as

$$k = \frac{4}{3}\sqrt{\frac{R_1R_2}{R_1+R_2}} \times \frac{\rho E_1E_2}{E_1(1-v_2^2)+E_2(1-v_1^2)} \tag{9}$$

where R_1 and R_2 are equivalent radius at the contact point of two contact bodies, mm. R_1 and R_2 replaced by the exterior transverse pitch circle radius of LSBG in this paper; ρ is the correction coefficient; v_1 and v_2 are the Poisson ratio of two materials; the materials of pinion and gear are No. 45# steel, so $v_1 = v_2 = 0.285$; E_1 and E_2 are, respectively, the elastic modulus of two materials, $E_1 = E_2 = 2.07\times105$ N/mm^2.

The expression of piecewise function Step(x,0,0,d,C) is shown as follows.

$$Step(x,x_0,h_0,x_1,h_1) = \begin{cases} h_0 & x \leq x_0 \\ h_0 + b(3-2\Delta)\Delta^2 & x_0 < x \leq x_1 \\ h_1 & x_1 < x \end{cases} \tag{10}$$

where $b = h_1-h_0$, mm ; $\Delta = (x-x_0)/(x_1-x_0)$; x is an independent variable, x_0, h_0 are the initial variable value and initial function value, respectively, x_1, h_1 are the end variable value and end function value, respectively.

The calculation expression for the contact distance x of the corresponding points on two simple rotate rigid bodies can be written as follows based on the Hertz elastic contact theory:

$$x = \sqrt[3]{\frac{9P^2(R_1+R_2)[E_1(1-v_2^2)+E_2(1-v_1^2)]^2}{16R_1R_2\rho^2{E_1}^2{E_2}^2}} \tag{11}$$

where P is the normal contact force of two contact bodies, N.

The contact stiffness coefficient k = 6.65×107 N/mm by putting corresponding data into Eqs. (8) and (9). The contact force index e = 1.5 according to the related literature [55-58]. The damping coefficient C = 50 N·s/mm. The contact maximum penetration depth d = 0.1 mm. The static friction coefficient is 0.08, and the dynamic friction coefficient is 0.05.

The gear theoretical angular velocity can be written by the equation according to the SBG transmission theory as follows:

$$n_2 = n_1 \times z_1/z_2 \tag{12}$$

where n_2 is the gear theoretical angular velocity, degree per

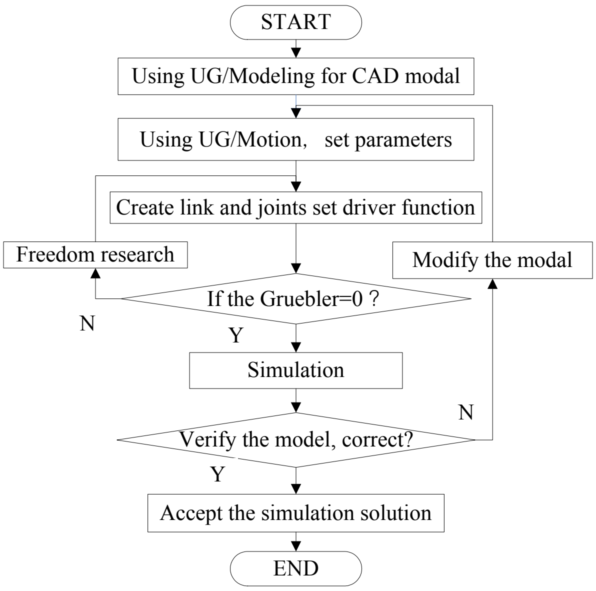

Fig. 7. The flow chart of dynamics simulation.

second; n_1 is the pinion input angular velocity, degree per second; z_1 is the number of pinion teeth, pcs; and z_2 is the number of gear teeth, pcs.

The theoretical angular velocity of the gear n_2 = 1873.703 degrees per second calculated by inputting corresponding data into Eq. (12).

Similarly, the theoretical numerical calculation formula for tangential contact force of bevel gear can be written as

$$F = \frac{2T}{d} \tag{13}$$

where F is the bevel gear tangential contact force, N; T is the transmitted torque, N·m; and d is the exterior transverse pitch circle diameter, mm.

The theoretical tangential contact force F = 23603.48 N is calculated by inputting corresponding data into Eq. (13).

3.2 Simulation flow and initialization

The dynamics simulation flow chart for SBG and LSBG meshing is shown in Fig. 7. The load for pinion's angular velocity is added by the step function. The pinion angular velocity is 7703 degrees per second, which is equivalent to 4500 revolutions per minute; the torque on the gear was 1964.99 Nm, which is the maximum output torque by engine through the transmission and main reducer. The simulation time is one second and the simulation steps are set to 500 steps. The meshing angular velocity and tangential contact force simulations were done for conventional SBG and LSBG under the same initial conditions, respectively.

The change curve of the pinion's angular velocity with time is shown in Fig. 8. A step function of angular velocity is added to the pinion; the pinion angular velocity maintains stabile at 7702.87 degrees per second after 0.2 seconds.

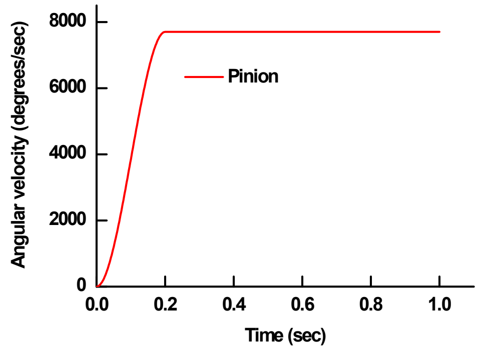

Fig. 8. The input angular velocity curve of the pinion.

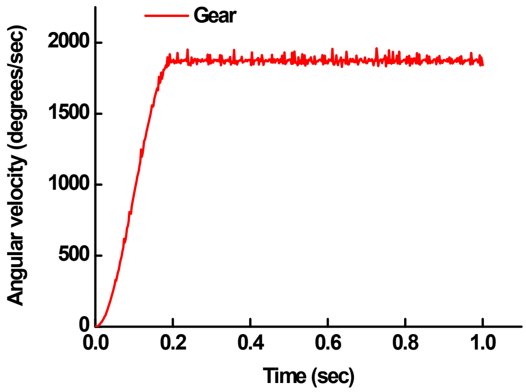

Fig. 9. The simulation angular velocity curve of the LSBG gear.

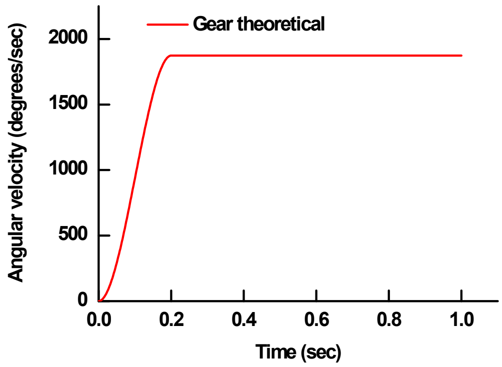

Fig. 10. The theoretical angular velocity curve of the LSBG gear.

3.3 Angular velocity simulation of the gear

The angular velocity simulation results of the gear are shown in Fig. 9. The angular velocity simulation average valve of the gear is 1873.77 degrees per second by calculation of simulation data after 0.2 seconds later.

Another theoretical angular velocity simulation of the gear is done by duplicate gear pair with the transmission ratio 9:37 in UG/motion software package. The change curve of the

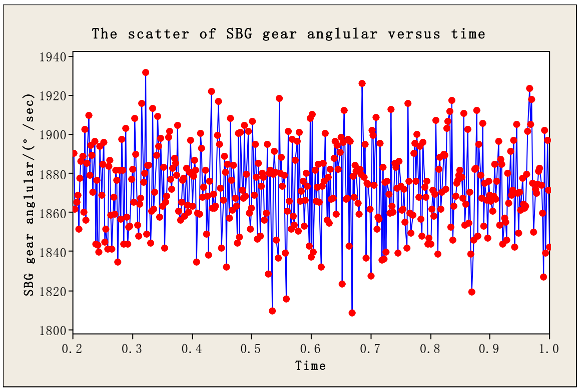

(a) SBG

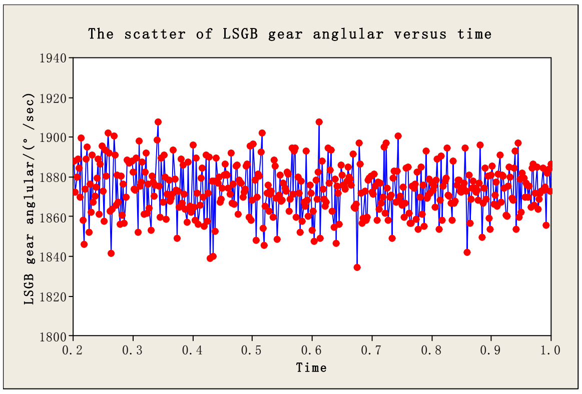

(b) LSBG

Fig. 11. The scatter diagram of gear angular velocity.

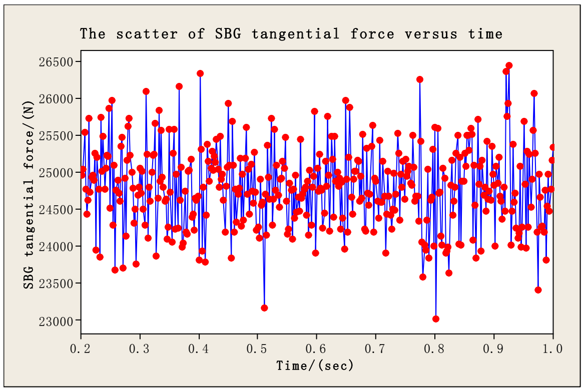

(a) SBG

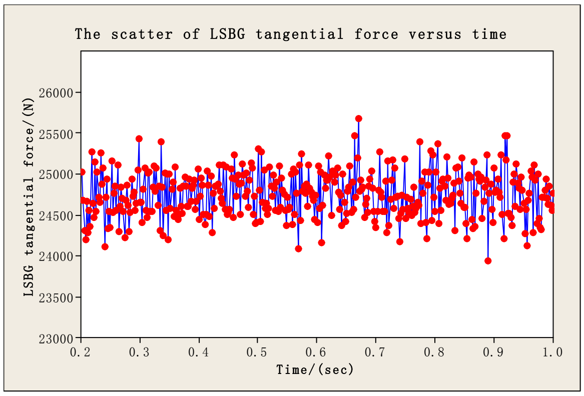

(b) LSBG

Fig. 12. The curve of tangential contact force.

gear's angular velocity with time is shown in Fig. 10. The angular velocity of the gear is a constant value at 1873.703 degrees per second after 0.2 seconds.

The curve of angular velocity simulation as shown in Fig. 9 goes into a stable state after 0.2 seconds later; the change amplitude scatter diagram after 0.2 seconds is shown in Fig. 11 with same coordinate axis scale for SBG and LSBG, Fig. 11(a) shows the SBG and Fig. 11(b) shows the LSBG. From the analysis graph, it shows that the change magnitude of the gear angular velocity for LSBG transmission is smaller than that of SBG under the same condition, that is to say the LSBG transmission is more stable.

3.4 Simulation of contact force

The change amplitude curve as shown in Fig. 12 with same coordinate axis scale for SBG and LSBG by extract the component force along the tangential direction of contact force between the pinion and the gear; Fig. 12(a) shows the SBG and Fig. 12(b) shows the LSBG. The average value of SBG tangential contact force is 24799.9N, while the average value of LSBG tangential contact force is 24747.5 N. It is clear that the change amplitude of tangential contact force for LSBG transmission is smaller than SBG when both are under the same condition.

4. The simulation data processing

4.1 The normality test and histogram of frequency distribution

There four groups data extracted from simulation data, respectively, are the angular velocity and tangential contact force of SBG, the angular velocity and tangential contact force of LSBG. Here we only consider the stable responses, which are 400 points data after 0.2 seconds. The normality test results of SBG and LSBG gear angular velocity are shown in Fig. 13. It can be seen that the scatters are basically in a straight line. The characteristics of SBG are shown in Fig. 13(a); the mean value of the gear's angular velocity is 1872.69 degrees per second, the standard deviation is 21.55 degrees per second, the Anderson-Darling statistics factor is 0.293 and obey normal distribution because of the value of $P = 0.601 > 0.05$. The characteristics of LSBG are shown in Fig. 13(b); the mean value of gear's angular velocity is 1873.77 degrees per second, the standard deviation is 12.67 degrees per second, the Anderson-Darling statistics factor is 0.264 and also obey normal distribution because of the value of $P = 0.697 > 0.05$.

The results of normality test for tangential contact force of SBG and LSBG are shown in Fig. 14. It can be seen that the scatters are basically in a straight line too. The characteristics of SBG are depicted by Fig. 14(a); the mean value of tangential contact force is 24799.9 N, the standard deviation is

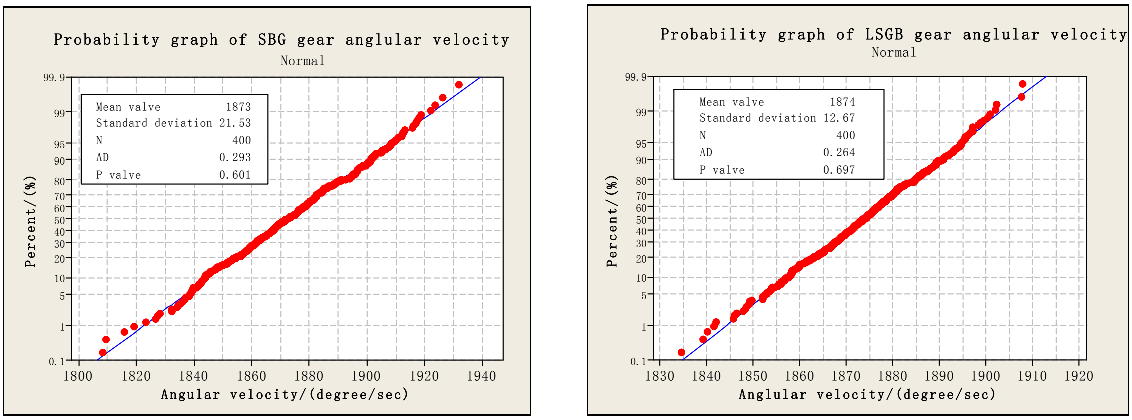

(a) SBG (b) LSBG

Fig. 13. Tests for normality of meshing angular velocity.

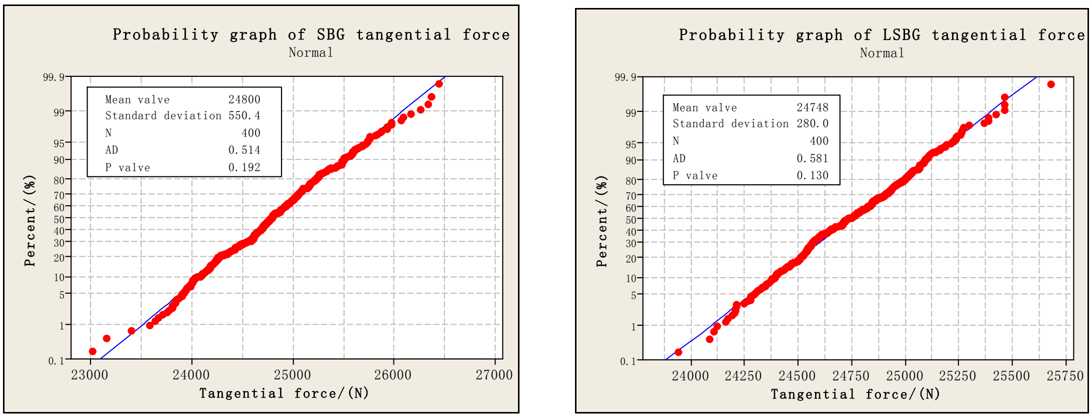

(a) SBG (b) LSBG

Fig. 14. Test of normality for tangential contact force.

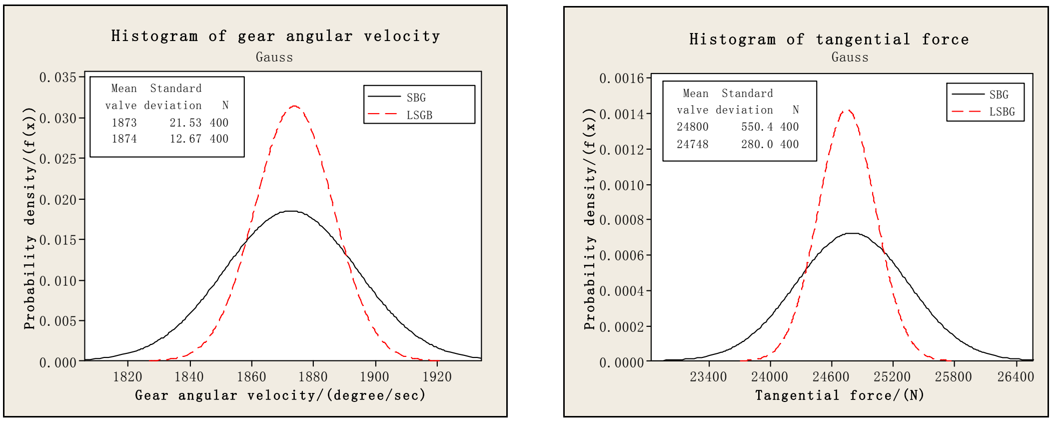

(a) Meshing angular velocity (b) Tangential contact force

Fig. 15. Frequency distribution histograms.

550.4 N, the Anderson-Darling statistics factor is 0.514, and obey normal distribution because of the value of $P = 0.192 > 0.05$. The characteristics of LSBG are shown by Fig. 14(b), the mean value of tangential contact force is 24747.5 N, the standard deviation is 280 N, the Anderson-Darling statistics factor is 0.581 and also obey normal distribution because of the value of $P = 0.130 > 0.05$.

There all obey normal distribution by the results of normality test for the angular velocity and tangential contact force of SBG and LSBG. The frequency distribution histograms are shown in Fig. 15. Standard deviation is a measure index which reflects the dispersion degree for average value of a set of data.

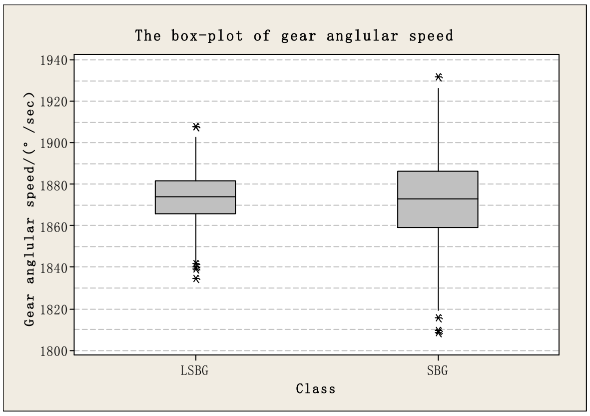

(a) Meshing angular velocity

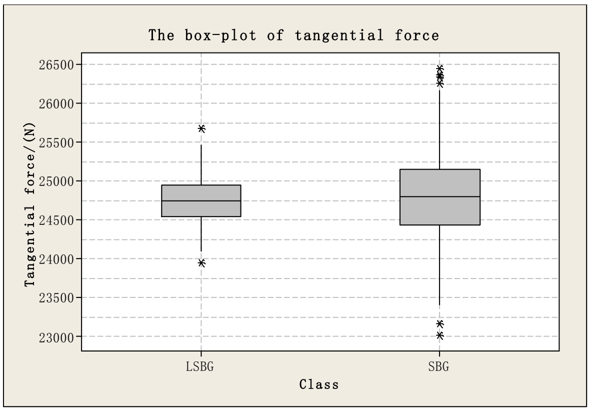

(b) Tangential contact force

Fig. 16. The box-plots.

It is shown that the standard deviation of SBG is larger than LSBG either meshing angular velocity or tangential contact force. The consistency and stability of LSBG meshing are superior to SBG, illustrated by standard deviation size as shown in Fig. 15 of the frequency distribution histogram.

4.2 The box-plot

Box-plot is a kind of statistical graph used to indicate the distribution characteristics of a group of data. The box-plot mainly contains five data lines: upper edge value line, upper quartile value line, median value line, lower quartile value line and lower edge value line. The box-plots of meshing angular velocity and tangential contact force are shown in Fig. 16. Fig. 16(a) is the box-plot of meshing angular velocity and Fig. 16(b) is the box-plot of tangential contact force. It is shown that the concentration performance of LSBG are superior to SBG both on meshing angular velocity and tangential contact force.

4.3 The average and range (X bar-R) control chart

The average and range control chart contains two charts. The above chart is the average control chart for monitoring of data center position [59-61] and the below chart is the range control chart for monitoring data dispersion degree. It reflects the center position and dispersion degree of a group of data [62-65]. According to the theory of probability and mathematical statistics knowledge, the distribution of sample average value obeys a normal distribution if the population data obeys a normal distribution. That is, $\bar{x} \sim N(\mu, \frac{\sigma^2}{n})$, (μ, σ are the mean value and standard deviation of the population data respectively). The dispersion range of $\bar{x}$ is $\mu \pm 3\sigma/\sqrt{n}$. Although the distribution of range R does not obey a normal distribution, the range R distribution still approximately obeys a normal distribution when sample capacity n < 10; thus the dispersion range of R is approximately $\bar{R} \pm 3\sigma_R$, ($\bar{R}$, σ_R are the mean value and standard deviation of range R respectively), and σ_R = dσ, d is a constant which can be found in Table 2.

Table 2. The values of parameters d, a_n, A_2, D_1, D_2.

Number for a group	d	a_n	A_2	D_1	D_2
4	0.880	0.486	0.73	2.28	0
5	0.864	0.430	0.58	2.11	0
6	0.848	0.395	0.48	2.00	0

The mean value μ and standard deviation σ of the population data are usually unknown. But the mean value μ of the population can be replaced by the average value $\bar{\bar{x}}$ of small sample average value $\bar{x}$ for parameter estimation. Similarly, the standard deviation σ of the population can be substituted for the small sample range value $a_n\bar{R}$ in parameter estimation.

$$\hat{\mu} = \bar{\bar{x}} = \frac{1}{k}\sum_{i=1}^{k}\bar{x}_i \tag{14}$$

$$\hat{\sigma} = a_n\bar{R} \tag{15}$$

$$\bar{R} = \frac{1}{k}\sum_{i=1}^{k}R_i \tag{16}$$

where $\hat{\mu}$ and $\hat{\sigma}$ are the estimate values of μ and σ, respectively; $\bar{x}_i$ is the average value of the sample; R_i is the range value of the sample and a_n is a constant with value from Table 2.

The three control lines of $\bar{x}$-R control chart are shown as follows:

For $\bar{x}$ chart: The center line

$$\bar{\bar{x}} = \frac{1}{k}\sum_{i=1}^{k}\bar{x}_i . \tag{17}$$

The upper control line

$$\bar{x}_s = \bar{\bar{x}} + A_2\bar{R} . \tag{18}$$

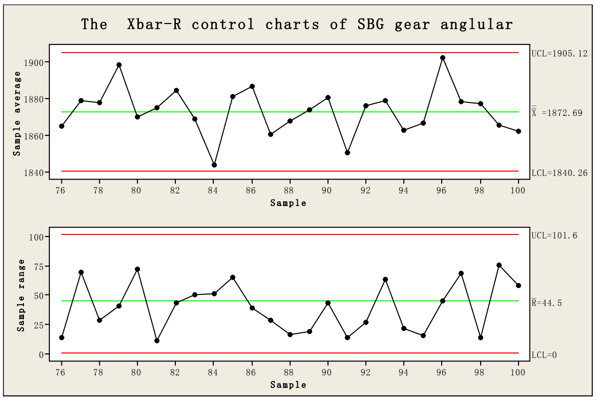

(a) SBG

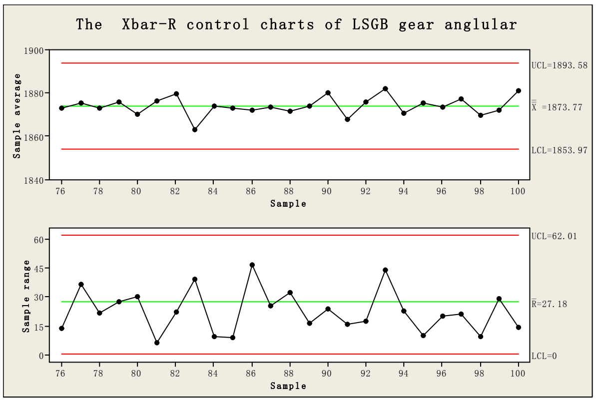

(b) LSBG

Fig. 17. The Xbar-R control charts for meshing angular velocity.

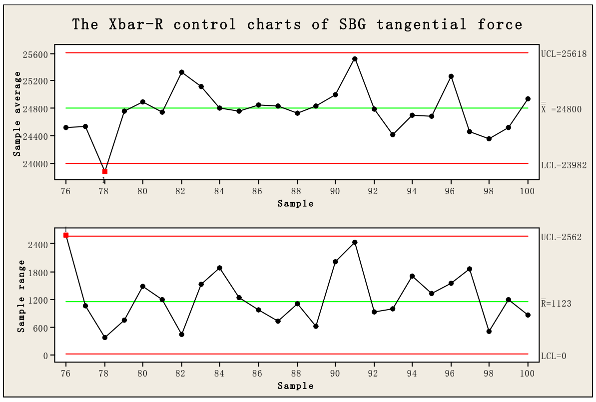

(a) SBG

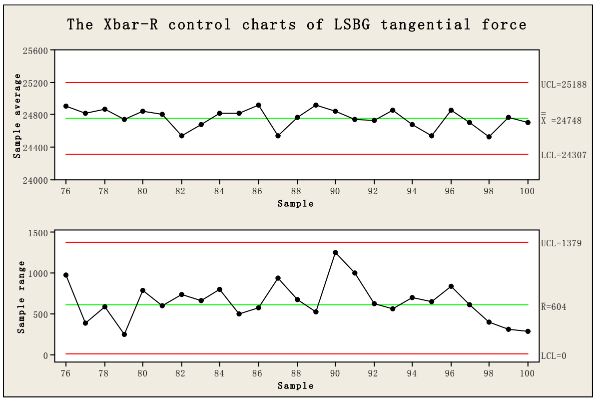

(b) LSBG

Fig. 18. The Xbar-R control charts for tangential contact force.

The lower control line

$$\bar{x}_x = \bar{\bar{x}} - A_2 \bar{R} \tag{19}$$

where A_2 is a constant, $A_2 = 3a_n / \sqrt{n}$, A_2 can be found in Table 2.

For R chart: The center line

$$\bar{R} = \frac{1}{k}\sum_{i=1}^{k} R_i \,. \tag{20}$$

The upper control line

$$R_s = \bar{R} + 3\sigma_R = (1 + 3da_n)\bar{R} = D_1\bar{R} \,. \tag{21}$$

The lower control line

$$R_s = \bar{R} - 3\sigma_R = (1 - 3da_n)\bar{R} = D_2\bar{R} \tag{22}$$

where D_1 and D_2 are constants with values from Table 2.

Take 100 points with range of 0.8-1.0 seconds as SBG and LSBG simulation data, divide them into 25 groups with 4 points for each, draw the meshing angular velocity $\bar{x}$-R control chart as shown in Fig. 17 with same coordinate axis scale for SBG and LSBG. Fig. 17(a) is the $\bar{x}$-R control chart of SBG meshing angular velocity in which the ninth point (the ninth data sets) mean value exceeds the lower control line, the twenty-first point is close to the upper control line, and the rest of the points are normal. Fig. 17(b) is the $\bar{x}$-R control chart of LSBG meshing angular velocity showing a normal fluctuation; no points exceed the control line. It is shown that the meshing angular velocity fluctuation of LSBG transmission is smaller than that of the SBG transmission. Thus; the stability of LSBG transmission is superior to that of SBG.

The $\bar{x}$-R control chart of tangential contact force of SBG and LSBG is drawn according to the 0.8-1.0 seconds simulation data as shown in Fig. 18 with same coordinate axis scale. Fig. 18(a) is SBG with the normal fluctuations, and Fig. 18(b) is LSBG also showing a normal fluctuation. The dispersion degree of tangential contact force of LSBG transmission is smaller than that of SBG obviously.

4.4 The comparison between simulation value and theoretical value of SBG and LSBG

The gear's theoretical meshing angular velocity and theoretical tangential contact force are calculated with Eqs. (12) and (13), respectively. The comparison between the simulation value and theoretical value is shown in Table 3.

For conventional SBG meshing, the relative error rate of the gear meshing angular velocity between simulation value and the theoretical calculation value is 0.054%, that is, the simulation model is very accurate for meshing angular velocity simu-

Table 3. The comparison between the simulation value and theoretical value of SBG and LSBG.

The type of SBG	Item for comparison	Simulation average value	The theoretical calculation values	Difference	Error rate
Conventional SBG	Meshing angular velocity /(degrees per second)	1872.69	1873.703	1.013	0.054%
	Tangential contact force /(N)	24799.9	23603.48	1196.42	4.82%
LSBG	Meshing angular velocity /(degrees per second)	1873.77	1873.703	0.067	0.0036%
	Tangential contact force /(N)	24747.5	23603.48	1144.02	4.85%

lation. The relative error of the tangential contact force between simulation value and theoretical calculation value is 4.82%.

For LSBG meshing, the relative error rate of the gear meshing angular velocity between simulation value and the theoretical calculation value is 0.0036%, emerges the advantages of the LSBG transmission with smaller angular velocity fluctuation, the transmission of LSGB is more stable. The relative error of the tangential contact force between simulation value and the theoretical calculation value is 4.85%. A way to reduce the error between simulation value and theoretical calculation value is to change related simulation parameters settings during simulation.

Generally, from the simulation of the SBG and LSBG, the error rates are in a range of engineering acceptable value which less than 5%. The simulation results are credible.

5. Conclusions

(1) A 3D geometric model and meshing model of LSBG are built according to the characteristics of LSBG which the tooth line is the conical logarithm spiral line and tooth profile is involutes by using the tooth flank equation deduction-discretization-surface fitting method.

(2) Simulation of meshing angular velocity and tangential contact force has been carried out based on the Hertz elastic contact theory. The calculation formula of contact force for SBG and LSBG meshing was expressed in the form of setting contact stiffness, contact force index, damping coefficient, penetration depth, static friction coefficient and kinetic friction coefficient.

(3) Simulations on meshing angular velocity and tangential contact force of LSBG pair and conventional SBG pair were successfully carried out by setting the initial parameters and other simulation parameters by use of UG/Motion software package. The conclusion is that LSBG transmission stability is superior to the conventional SBG drown by the results comparisons of SBG and LSBG simulation in meshing angular velocity and tangential contact force.

(4) The simulations may pave the way for LSBG design and manufacture for applications in industry, also contributing to subsequent tasks like computer aided engineering analysis, the process and machining of prototype.

The parametric modeling of the LSBG as well as the machining for the product is still future work.

Acknowledgments

This work supported by the National Natural Science Foundation of China under grant No.51475399, No.51375411 and the Science and Technology Projects JA14240 of Education Department of Fujian Province, China.

Nomenclature

SBG : Spiral bevel gear
LSBG : Logarithmic spiral bevel gear
3D : Three dimensional
α : Half angle of cone
β : Spiral angle
F : Contact force
K : Coefficient of the contact stiffness
x : Distance of two contact bodies
e : Contact force index
C : Damping coefficient
d : Contact maximum penetration depth
R_1 R_2 : Equivalent radius at the contact point
ρ : Correction coefficient
v_1 v_2 : Poisson ratio of two materials
E_1 E_2 : Elastic modulus
n_1 : Pinion input angular velocity
n_2 : Gear theoretical angular velocity
z_1 : Number of pinion teeth
z_2 : Number of gear teeth
T : Transmitted torque
D : Exterior transverse pitch circle diameter

References

[1] T. Zeng, *The design and manufacture of spiral bevel gear*, Harbin: Harbin Institute of Technology Press (1989) 213-218 (In Chinese).

[2] Q. Li and H. B. Yan, *The Logarithmic spiral bevel gear meshing theory*, Beijing: Metallurgical Industry Press (2012) (In Chinese).

[3] G. Q. Song, *Logarithmic spiral bevel gear and the gear machining with logarithmic spiral cam: China*, 95104630.6 (1996) (In Chinese).

[4] Q. Li, G. P. Wang and H. S. Weng, Study on gearing theory of logarithmic spiral bevel gear, *3rd WSEAS International Conference on Applied and Theoretical Mechanics*, Spain (2007)

(12) 14-16.
[5] H. Ding and H. A. S. Y. Z. Dan, Method of spiral bevel gear modeling and its prospect, *Mechanical Design and Manufacturing*, 51 (1) (2014) 257-260 (In Chinese).
[6] Y. C. Tsai and W. Y. Hsu, The study on the design of spiral bevel gear sets with circular-arc contact paths and tooth profiles, *Mechanism and Machine Theory*, 43 (9) (2008) 1158-1174.
[7] B. Jerzy et al., 3D modeling of induction hardening of gear wheels, *J. of Computational and Applied Mathematics*, 270 (11) (2014) 231-240.
[8] S. H. Chen and Z. H. Fong, Study on the cutting time of the hypoid gear tooth flank, *Mechanism and Machine Theory*, 84 (2) (2015) 113-124.
[9] H. T. Li et al., The kinematic synthesis of involute spiral bevel gears and their tooth contact analysis, *Mechanism and Machine Theory*, 79 (9) (2014) 141-157.
[10] C. H. Lin and Z. H. Fong, Numerical tooth contact analysis of a bevel gear set by using measured tooth geometry data, *Mechanism and Machine Theory*, 84 (2) (2015) 1-24.
[11] J. Y. Tang, T. P. Pu and J. Dai, The study of spiral bevel gear geometry modeling method of SGM processing, *Mechanical Transmission*, 32 (1) (2008) 43-46+83 (In Chinese).
[12] Y. W. Sun, H. J. Liu and J. Liu, Study on free surface accurately fitting method based on NURBS, *Chinese J. of Mechanical Engineering*, 40 (3) (2005) 10-14 (In Chinese).
[13] W. Wei and L. H. Zhang, Spiral bevel gear's modeling and rounded tip and undercutting, *Mechanical Design*, 28 (3) (2011) 9-12 (In Chinese).
[14] Y. W. Xu and L. H. Zhang, Virtual machining on monolithic structure spiral bevel gear milling machine, *Transactions of the CSAE*, 24 (12) (2008) 71-75.
[15] Q. Fan, Computerized modeling and simulation of spiral bevel and hypoid gears manufactured by Gleason face hobbing process, *J. of Mechanical Design*, 128 (11) (2005) 1315-1327.
[16] F. L. Litvin et al., An invariant approach for gear generation with supplemental motions, *Mechanism and Machine Theory*, 42 (3) (2007) 275-295.
[17] W. L. Chen and C. B. Tsay, Mathematical model and tooth surfaces of recess action worm gears with double-depth teeth, *Mechanism and Machine Theory*, 46 (12) (2011) 1840-1853.
[18] K. Y. Chen and C. B. Tsay, Mathematical model and worm wheel tooth working surfaces of the ZN-type hourglass worm gear set, *Mechanism and Machine Theory*, 44 (9) (2009) 1701-1712.
[19] M. Vimercati, Mathematical model for tooth surfaces representation of face-hobbed hypoid gears and its application to contact analysis and stress calculation, *Mechanism and Machine Theory*, 42 (6) (2007) 668-690.
[20] Y. M. Cui, Z. D. Fang and J. Z. Su, Precise modeling of arc tooth face-gear with transition curve, *Chinese J. of Aeronautics*, 26 (5) (2013) 1346-1351.
[21] J. C. Li et al., Precise entity spiral bevel gear manufacture method and meshing theory based modeling, *J. of Jilin University: Engineering Science*, 38 (6) (2008) 1315-1319 (In Chinese).
[22] H. Y. Fang, S. R. Hong and J. H. Yang, Modeling and Simulation of Klingelnberg spiral bevel gear, *J. of Huaqiao University (Natural Science Edition)*, 25 (1) (2004) 67-70 (In Chinese).
[23] H. F. Chen, J. Y. Tang and W. Zhou, Modeling and predicting of surface roughness for generating grinding gear, *J. of Materials Processing Technology*, 213 (5) (2013) 717-721.
[24] H. S. Javed and K. J. Neelesh, Modeling of material removal rate and surface roughness in finishing of bevel gears by electrochemical honing process, *J. of Materials Processing Technology*, 214 (2) (2014) 200-209.
[25] M. Li and H. Y. Hu, Dynamic analysis of a spiral bevel-geared rotor-bearing system, *J. of Sound and Vibration*, 259 (3) (2003) 605-624.
[26] T. Osman and P. Velex, A model for the simulation of the interactions between dynamic tooth loads and contact fatigue in spur gears, *Tribology International*, 46 (1) (2012) 84-96.
[27] H. J. Jiang, Y. M. Shao and C. K. Mechefske, Dynamic characteristics of helical gears under sliding friction with spalling defect, *Engineering Failure Analysis*, 39 (4) (2014) 92-107.
[28] T. Eritenel and R. G. Parker, An investigation of tooth mesh nonlinearity and partial contact loss in gear pairs using a lumped-parameter model, *Mechanism and Machine Theory*, 56 (10) (2012) 28-51.
[29] F. Alfonso, R. Q. Ramon and G. P. Ignacio, Computerized design, simulation of meshing, and finite element analysis of two types of geometry of curvilinear cylindrical gears, *Comput. Methods Appl. Mech. Engrg*., 272 (4) (2014) 321-339.
[30] D. R. Houser and J. Borner, Friction and bending moments as gear noise excitations, *SAE Transactions*, 105 (6) (1996) 1669-1676 (paper Number: 961816).
[31] A. Kahraman, Effect of axial vibrations on the dynamics of a helical gear pair, *J. of Vibration and Acoustics*, 115 (1) (1993) 33-39.
[32] T. Nishino, Vibration analysis of the helical gear system using the integrated excitation model, *JSME J. of Advanced Mechanical Design, Systems, and Manufacturing*, 1 (4) (2007) 541-552.
[33] G. W. Blankenship and R. Singh, A new gear mesh interface dynamic model to predict multi-dimensional force coupling and excitation, *Mechanism and Machine Theory*, 30 (1) (1995) 43-57.
[34] T. Nishino, Integrated excitation models of the helical gear system, *ASME Design Engineering Technical Conferences*, no. DETC2007-34134, Las Vegas, NV (2007).
[35] F. L. Litvin, A. G. Wang and R. F. Handschuh, Computerized generation and simulation of meshing and contact of spiral bevel gears with improved geometry, *Computer Methods in Applied Mechanics and Engineering*, 158 (3) (1998) 35-64.
[36] F. L. Litvin et al., Integrated computer program for simulation of meshing and contact of gear drives, *Computer Methods in Applied Mechanics and Engineering*, 181 (2) (2000) 71-85.
[37] P. Y. Wang and Z. H. Fong, Fourth-order kinematic synthesis for face-milling spiral bevel gears with modified radial motion (MRM) correction, *J. of Mechanical Design (ASME)*, 128 (3) (2006) 457-467.
[38] L. G. Yao et al., Mathematical modeling and simulation of the external and internal double circular-arc spiral bevel gears for

the nutation drive, *J. of Mechanical Design (ASME)*, 132 (2) (2010) 1-10.
[39] X. Gu and P. Velex, On the dynamic simulation of eccentricity errors in planetary gears, *Mechanism and Machine Theory*, 61 (1) (2013) 14-29.
[40] Z. G. Chen and Y. M. Shao, Dynamic simulation of spur gear with tooth root crack propagating along tooth width and crack depth, *Engineering Failure Analysis*, 18 (8) (2011) 2149-2164.
[41] Z. G. Chen and Y. M. Shao, Dynamic simulation of planetary gear with tooth root crack in ring gear, *Engineering Failure Analysis*, 31 (6) (2013) 8-18.
[42] Z. G. Chen, Y. M. Shao and D. Z. Su, Dynamic simulation of planetary gear set with flexible spur ring gear, *J. of Sound and Vibration*, 332 (26) (2013) 7191-7204.
[43] Y. M. Cui et al., Precise modeling of arc tooth face-gear with transition curve, *Chinese J. of Aeronautics*, 26 (5) (2013) 1346-1351.
[44] F. Benamar and C. Grand, Quasi-static motion simulation and slip prediction of articulated planetary rovers using a kinematic approach, *J. of Mechanisms and Robotics (ASME)*, 5 (3) (2013) 1-13.
[45] V. V. Simon, Manufacture of optimized face-hobbed spiral bevel gears on computer numerical control hypoid generator, *J. of Manufacturing Science and Engineering (ASME)*, 136 (6) (2014) 1-9.
[46] W. J. Qin and C. Y. Guan, An investigation of contact stresses and crack initiation in spur gears based on finite element dynamics analysis, *International J. of Mechanical Sciences*, 83 (6) (2014) 96-103.
[47] I. Atanasovska, The mathematical phenomenological mapping in non-linear dynamics of spur gear pair and radial ball bearing due to the variable stiffness, *International J. of Non-Linear Mechanic*, 73 (7) (2015) 114-120.
[48] J. H. Xue, W. Li and C. Y. Qin, The scuffing load capacity of involute spur gear systems based on dynamic loads and transient thermal elastohydrodynamic lubrication, *Tribology International*, 79 (11) (2014) 74-83.
[49] S. Patil et al., Contact stress analysis of helical gear pairs, including frictional coefficients, *International J. of Mechanical Sciences*, 85 (8) (2014) 205-211.
[50] H. J. Jiang, Y. M. Shao and C. K. Mechefske, Dynamic characteristics of helical gears under sliding friction with spalling defect, *Engineering Failure Analysis*, 39 (4) (2014) 92-107.
[51] T. M. Ericson and R. G. Parker, Experimental measurement of the effects of torque on the dynamic behavior and system parameters of planetary gears, *Mechanism and Machine Theory*, 74 (4) (2014) 370-389.
[52] S. J. Tsai, G. L. Huang and S. Y. Ye, Gear meshing analysis of planetary gear sets with a floating sun gear, *Mechanism and Machine Theory*, 84 (2) (2015) 145-163.
[53] Y. Guo, J. Keller and R. G. Parker, Nonlinear dynamics and stability of wind turbine planetary gear sets under gravity effects, *European J. of Mechanics A/Solids*, 47 (9) (2014) 45-57.
[54] F. R. Bi, X. T. Cui and Y. Liu, Computer simulation for dynamic meshing force of involute gear, *J. of Tianjin University*, 38 (11) (2005) 991-995 (In Chinese).
[55] Z. H. Huang, X. J. Zhan and Y. Z. Zhou, Contact force of involute gear meshing simulation, *J. of Central South University (Natural Science Edition)*, 42 (2) (2011) 379-383 (In Chinese).
[56] S. Q. Lu, Theoretical analysis and Simulation of contact force multi gear variable gear pump, *J. of Hydraulic and Pneumatic*, 37 (2) (2014) 101-104 (In Chinese).
[57] Z. G. Wan et al., An improved time-varying mesh stiffness algorithm and dynamic modeling of gear-rotor system with tooth root crack, *Engineering Failure Analysis*, 42 (7) (2014) 157-177.
[58] T. J. Lin et al., A finite element method for 3D static and dynamic contact impact analysis of gear drives, *Comput. Methods Appl. Mech. Engrg*., 196 (9) (2007) 1716-1728.
[59] Z. Wu and M. Y. Michael, What are the best sample sizes for the X-bar and CUSUM charts, *Int. J. Production Economics*, 31 (1) (2011) 650-662.
[60] M. C. Chih, L. L. Yel and F. C. Li, Particle swarm optimization for the economic and economic statistical designs of the X-bar control chart, *Applied Soft Computing*, 11 (8) (2011) 5053-5067.
[61] A. Ganguly and S. K. Patel, A teaching-learning based optimization approach for economic design of X-bar control chart, *Applied Soft Computing*, 24 (11) (2014) 643-653.
[62] M. H. Shu and H. C. Wu, Fuzzy X and R control charts: Fuzzy dominance approach, *Computers and Industrial Engineering*, 61 (3) (2011) 676-685.
[63] S. Ali and M. Riaz, Cumulative quantity control chart for the mixture of inverse Rayleigh process, *Computers and Industrial Engineering*, 73 (7) (2014) 11-20.
[64] L. P. Liu et al., Economic and economic-statistical designs of an X control chart for two-unit series systems with condition-based maintenance, *European J. of Operational Research*, 226 (3) (2013) 491-499.
[65] M. Bashiri et al., Multi-objective genetic algorithm for economic statistical design of X control chart, *Scientia Iranica E*, 20 (3) (2013) 909-918.

Tieming Xiang received his B.S. and M.S. from South China University of Technology in 2002 and 2008, respectively. He is currently a doctoral student at College of Mechanical Engineering and Automation, Huaqiao University, China, his research interests include mechanical dynamics and CAE.

Lizhi Gu received his B.S, M.S. and Ph.D at Harbin Institute of Technology in 1982, 1990 and 2000, respectively. Currently, he is a Professor at Huaqiao University, China. His research interests include metal cutting and advanced manufacturing technology, CAD / CAPP / FMS and digital design and manufacturing.